The Astrophysical Journal, 965:146 (12pp), 2024 April 20 https://doi.org/10.3847/1538-4357/ad2dfe

Ultra-relativistic Electron Acceleration during High-intensity Long-duration Continuous Auroral Electrojet Activity Events

Rajkumar Hajra[1], Bruce T. Tsurutani[6], Quanming Lu[1], Gurbax S. Lakhina[7], Aimin Du[2], Ezequiel Echer[3], Adriane M. S. Franco[4], Mauricio J. A. Bolzan[5], and Xinliang Gao[1]
[1] CAS Key Laboratory of Geospace Environment, School of Earth and Space Sciences, University of Science and Technology of China, Hefei, People's Republic of China; rajkumarhajra@yahoo.co.in, rhajra@ustc.edu.cn
[2] College of Earth and Planetary Sciences, Chinese Academy of Sciences, Beijing, People's Republic of China
[3] Instituto Nacional de Pesquisas Espaciais, São José dos Campos, Brazil
[4] Universidade Federal do Sul e Sudeste do Para, Maraba, Brazil
[5] Universidade Federal de Jatai, Jatai, Brazil
Received 2023 October 8; revised 2024 February 20; accepted 2024 February 22; published 2024 April 16

Abstract

Magnetospheric relativistic electrons are accelerated during substorms and strong convection events that occur during high-intensity long-duration continuous auroral electrojet activity (HILDCAA) events, associated with solar wind high-speed streams (coming from coronal holes). From an analysis of ∼2–20 MeV electrons at $L \sim 2$–7 measured by the Van Allen Probe satellite, it is shown that ∼3.4–4.1 days long HILDCAA events are characterized by ∼7.2 MeV electron acceleration in the $L \sim 4.0$–6.0 region, which occurs ∼2.9–3.4 days after the onset of HILDCAA. The dominant acceleration process is due to wave–particle interactions between magnetospheric electromagnetic chorus waves and substorm-injected ∼100 keV electrons. The longer the HILDCAA and chorus last, the higher the maximum energy of the accelerated relativistic electrons. The acceleration to higher and higher energies is due to a bootstrap mechanism.

Unified Astronomy Thesaurus concepts: Van Allen radiation belts (1758); Interplanetary magnetic fields (824); Interplanetary medium (825); Solar storm (1526); Solar coronal mass ejections (310); Solar activity (1475)

1. Introduction

High-intensity long-duration continuous auroral electrojet activity (HILDCAA; Tsurutani & Gonzalez 1987) events represent intense geomagnetic activities in the auroral region without developments of significant magnetospheric storm time ring currents (Guarnieri 2006; Hajra et al. 2013, 2014a; Souza et al. 2016; Mendes et al. 2017; Guarnieri et al. 2018; Souza et al. 2018; Hajra et al. 2020; Hajra 2021a). They are shown to occur during solar wind high-speed streams (HSSs) emanating from coronal holes (Hajra et al. 2013). HILDCAA is characterized by long and sporadic substorm and DP2 (disturbance polar) activities (which are counterparts of the convective system generated in the global magnetosphere; Nishida 1968). HILDCAA has been shown (Hajra et al. 2015a) to be associated with enhanced electromagnetic chorus waves (Tsurutani & Smith 1977; Meredith et al. 2001; Tsurutani et al. 2010, 2013) in the $5 < L < 10$ region between 0 and 12 magnetic local time, and flux enhancements of relativistic >0.6, >2, and >4 MeV electrons at geosynchronous orbit ($L = 6.6$). The McIlwain L is the distance in Earth radius (R_E) for a dipole magnetic field line to cross the magnetic equatorial plane (McIlwain 1961). During HILDCAA, ∼10–100 keV electrons are injected into the nightside magnetosphere (DeForest & McIlwain 1971; Horne & Thorne 1998). Temperature anisotropy of the injected electrons leads to the creation of chorus waves by a whistler-mode plasma instability (Kennel & Petschek 1966; Tsurutani & Smith 1977; Tsurutani et al. 1979; Tsurutani & Lakhina 1997; Meredith et al. 2001; Lu et al. 2019). The chorus waves accelerate the energetic ∼100 keV electrons to >0.6 MeV electrons through cyclotron resonant interactions (Inan et al. 1978; Horne & Thorne 1998; Horne et al. 2003; Thorne et al. 2005; Tsurutani et al. 2006a; Summers et al. 2007; Reeves et al. 2013; Thorne et al. 2013; Boyd et al. 2014). In a bootstrap mechanism (Hajra et al. 2015a), these >0.6 MeV electrons are accelerated to >2 MeV and then to >4 MeV electrons through further wave–particle interactions. Tsurutani et al. (2009) showed that chorus waves are coherent, making them more efficient in accelerating MeV electrons (Green & Kivelson 2004; Lakhina et al. 2010; Bellan 2013; Mourenas et al. 2018; Yoon & Bellan 2020).

Another competing mechanism for electron acceleration is radial diffusion caused by interaction with ultralow frequency quasi-sinusoidal continuous pulsations (Pc5s). In this mechanism, diffusion of electrons from the outer magnetosphere with weak magnetic fields to the inner magnetosphere with stronger magnetic fields results in betatron and Fermi accelerations of the electrons (Alfvén 1950; Fälthammar 1965; Schulz & Lanzerotti 1974; Elkington et al. 1999; Hudson et al. 1999; Li & Temerin 2001; Mann et al. 2004; Miyoshi et al. 2004). Earlier works have demonstrated case-to-case variations in the dominant roles played by radial diffusion (Zong et al. 2009; Ali et al. 2016; Jaynes et al. 2018; Ozeke et al. 2020) and local acceleration (Thorne 2010; Reeves et al. 2013; Thorne et al. 2013; Li et al. 2014; Xiao et al. 2014; Allison & Shprits 2020; Guo et al. 2021). The combined impacts of both the mechanisms (Baker et al. 2014; Zhao et al. 2019; Guo et al. 2023) and energy-dependent acceleration mechanisms (Foster et al. 2014; Kanekal et al. 2015; Li et al. 2016; Zhao et al. 2018) have also been discussed.

[6] Retired, Pasadena, California, USA.
[7] Retired, Vashi, Navi Mumbai, India.

Table 1
Relativistic Electron Acceleration by ⩾2 Orders of Magnitude during HILDCAA

HILDCAA						HSS $V_{sw} > 500$ km s^{-1}		Electron Acceleration		
Year	Start	End	Duration (day)	AE_p[a] (nT)	IAE[b] (nT day)	Peak V_{sw} (km s^{-1})	Duration (day)	E_{max}[c] (MeV)	Delay[d] (day)	L Shell
2016	Nov 24 00:00	Nov 26 12:03	2.50	1837	1021	726	2.94	5.6	2.31	4.5–6.0
2016	**Dec 21 09:41**	**Dec 24 18:57**	**3.39**	**2231**	**1381**	**775**	**6.64**	**7.2**	**3.04**	**4.0–6.0**
2017	**Jan 31 08:34**	**Feb 4 01:01**	**3.69**	**1440**	**1285**	**773**	**4.60**	**7.2**	**3.37**	**4.0–5.5**
2017	**Aug 21 07:28**	**Aug 21 10:24**	**4.12**	**1847**	**1777**	**769**	**5.06**	**7.2**	**2.93**	**4.0–5.6**
2019	Feb 1 02:39	Feb 3 07:48	2.21	1262	658	661	2.54	4.5	2.17	5.0–6.0
2019	Feb 28 05:51	Mar 2 19:25	2.57	1280	1014	627	2.85	5.6	2.14	5.0–6.0

Notes.
[a] AE_p: the peak AE value.
[b] IAE: integrated AE value.
[c] E_{max} refers to the maximum energy of the electrons during HILDCAA.
[d] Delay refers to the time from the onset of HILDCAA to the onset of flux acceleration. The cases showing acceleration up to ∼7.2 MeV electrons are marked in bold font.

However, no such comparative studies of electron acceleration mechanisms have been reported for HILDCAA.

The previous MeV electron variability studies during HILDCAA were limited in electron energies (>0.6, >2, and >4 MeV) and only at geosynchronous orbit observations (Hajra et al. 2014b, 2015a, 2015b; Tsurutani et al. 2016a). Recent studies using Van Allen Probe (VAP; Mauk et al. 2013) measurements and simulations have confirmed the important roles of continuous, strong substorms and convection events play on the acceleration of relativistic electrons (e.g., Mourenas et al. 2019; Hajra 2021b; Hua et al. 2022a, 2022b; Mourenas et al. 2022). However, the upper energy limit up to which electrons may be accelerated during HILDCAA, and the magnetospheric region of the most effective acceleration process, are not understood at present. In this effort, we will study ∼2–20 MeV electron flux variations in the entire outer radiation belt ($L \sim 2$–7) measured by VAPs to understand the relativistic electron variations associated with HILDCAA. In addition, acceleration mechanisms of the electrons will be verified using the electron phase space density (PSD) radial profiles and wave observations by the VAP instrumentations. This work will hopefully advance our present understanding of relativistic electron convection, acceleration, and diffusion in the magnetosphere.

2. Data and Methods

HILDCAA events are identified following the strict HILDCAA criteria (Tsurutani & Gonzalez 1987): auroral electrojet (AE) activity with an AE peak >1000 nT (high intensity) continuing for >2 days (long duration) when AE does not fall below 200 nT for >2 hr at a time (continuous), occurring during geomagnetic quiet conditions or geomagnetic storm recovery phases. From the AE temporal variations, the intervals with the AE peak >1000 nT were first identified. Then AE time series were scanned both forward and backward in time to determine where AE decreased below 200 nT for ⩾2 hr. If this interval was >2 days long, and was outside of a magnetic storm (SYM-H < −50 nT: Akasofu 1981; Gonzalez et al. 1994), it was identified as an HILDCAA event.

For each of the HILDCAA events, the characteristic AE peak value, duration, and time-integrated AE intensity are estimated. The maximum AE value during HILDCAA is defined as the characteristic AE peak value of the event. The integrated AE is computed from the area under the AE temporal curve, and expressed in the unit of nanotesla times day or nanotesla day. The geomagnetic AE and SYM-H indices are obtained from the World Data Center for Geomagnetism, Kyoto, Japan.[8]

As one goal of this work is to study the MeV electron L-shell variations during HILDCAA, we only considered HILDCAA events when suitable VAP MeV electron observations are available. Under this constraint, we selected six isolated HILDCAA events during the entire VAP operation period, from 2012 August to 2019 October, when radiation belt energization could be studied without potential contamination from other geomagnetic effects. The events are listed in Table 1.

The main data of this work are the VAP ∼2–20 MeV electron flux intensities and variations. The L-shell variations in the spin-averaged relativistic (∼2–3 MeV) and ultra-relativistic (>3 MeV) electron fluxes are measured by the Relativistic Electron Proton Telescope instrument (Baker et al. 2013).

To study the magnetospheric chorus wave activity, typically with frequency (0.05–0.8) f_{ce} (Tsurutani & Smith 1977), we explored the wave magnetic fields measured by the Electric and Magnetic Field Instrument Suite and Integrated Science instrument (Kletzing et al. 2013). f_{ce} is the electron cyclotron frequency.

Electron PSDs are explored to understand the acceleration processes of the relativistic and ultra-relativistic electrons (Morley et al. 2013; Schiller et al. 2017). PSDs are calculated from the observed directional differential electron fluxes j: $f = j/p^2$ (where p is the electron momentum). The Tsyganenko 04 storm time model (Tsyganenko & Sitnov 2005) was used to express the electron PSDs in terms of the three adiabatic invariants of the particle motion in the geomagnetic field, μ, K, and L^* (Schulz & Lanzerotti 1974), to remove the adiabatic variations and reveal the true electron acceleration. μ is the first adiabatic invariant corresponding to electron gyrational motion about the magnetic field. K corresponds to bounce motion along the field lines, and is a combination of the first two adiabatic invariants. It is independent of the particle mass and charge, and is invariant only in the absence of field-aligned electric fields. L^* corresponds to drift motion around Earth, and

[8] https://wdc.kugi.kyoto-u.ac.jp/

is commonly referred to as the Roederer L related to the third adiabatic invariant (Roederer 1970).

The study of the electron PSDs can clearly distinguish between two electron acceleration processes, namely, radial diffusion and local acceleration (Reeves et al. 2013). A monotonically increasing PSD with increasing L^* (keeping μ and K constant) is an indication of a radial diffusion that moves electrons from higher PSD or a source population at high L^* to lower PSD region at lower L^*. It was recently reported (Olifer et al. 2021) that monotonic PSD profiles that are rapidly increasing due to acceleration from very fast inward radial diffusion may result in an apparent PSD peak. On the other hand, radially localized growing PSD peaks and negative gradients at higher L^* essentially indicate a local electron acceleration process (e.g., Boyd et al. 2018; Allison & Shprits 2020). All VAP data are collected from the VAP Science Gateway.[9]

In order to study the near-Earth solar wind and interplanetary conditions, solar wind plasma and interplanetary magnetic field (IMF) data are collected from the OMNI web.[10] These are based on measurements by the Advanced Composition Explorer, Wind, Interplanetary Monitoring Platform 8, and Geotail spacecraft upstream of the Earth, and shifted to the Earth's bow shock nose. The IMF components are given in the Geocentric Solar Magnetospheric coordinates, where the x-axis is directed toward the Sun, and the y-axis is in the $\boldsymbol{\Omega} \times \hat{\boldsymbol{x}}/|\boldsymbol{\Omega} \times \hat{\boldsymbol{x}}|$-direction, $\hat{\boldsymbol{x}}$ is the unit vector along the x-axis, and $\boldsymbol{\Omega}$ is aligned with the magnetic south-pole axis of Earth. The z-axis completes a right-hand system.

3. Results and Discussion

Figures 1(a)–(h) show the variations in relativistic and ultra-relativistic electron fluxes associated with an HILDCAA event occurring during 2019 February 1–3. The blue bar in the AE panel (Figure 1(k)) marks the interval consistent with the classical HILDCAA criteria (Tsurutani & Gonzalez 1987). The HILDCAA has a duration of ∼2.21 days, an AE peak of 1262 nT, and an integrated AE value of ∼658 nT day.

The near-Earth solar wind plasma and IMF variations (Figures 1(i)–(j)) indicate a corotating interaction region (CIR; Smith & Wolfe 1976; Tsurutani et al. 2006b) preceding the onset of HILDCAA. The CIR is characterized by a compressed IMF with an amplitude B_0 of ∼19.7 nT, and a peak proton density N_p of ∼44.7 cm^{-3} (see Hajra & Sunny 2022; Hajra et al. 2022; Sunny et al. 2023 for typical CIR characteristic parameters). It is located between a slow stream with speed V_{sw} of ∼290–430 km s^{-1} on January 28–30, and an HSS with V_{sw} of ∼530–660 km s^{-1} on February 2–3. The HSS interval with $V_{sw} > 500$ km s^{-1} has a duration of ∼2.54 days. Both the CIR and the HSS are embedded with fluctuating IMF components (Figure 1(j)). They represent nonlinear Alfvén waves (Belcher & Davis 1971; Tsurutani et al. 1995, 2005, 2006a, 2006b). The HILDCAA resulted from the magnetospheric reconnection (Dungey 1961; Tsurutani & Meng 1972) between the Alfvén wave IMF southward component B_s and the northward geomagnetic field (Tsurutani & Gonzalez 1987; Tsurutani et al. 1990, 1995).

At the onset of HILDCAA, relativistic ∼2.0–2.9 MeV electron fluxes are depleted from the magnetosphere at $L \geqslant 4$ (Figures 1(a)–(c)). The electron depletion may be explained by two possible mechanisms: (1) due to a magnetopause

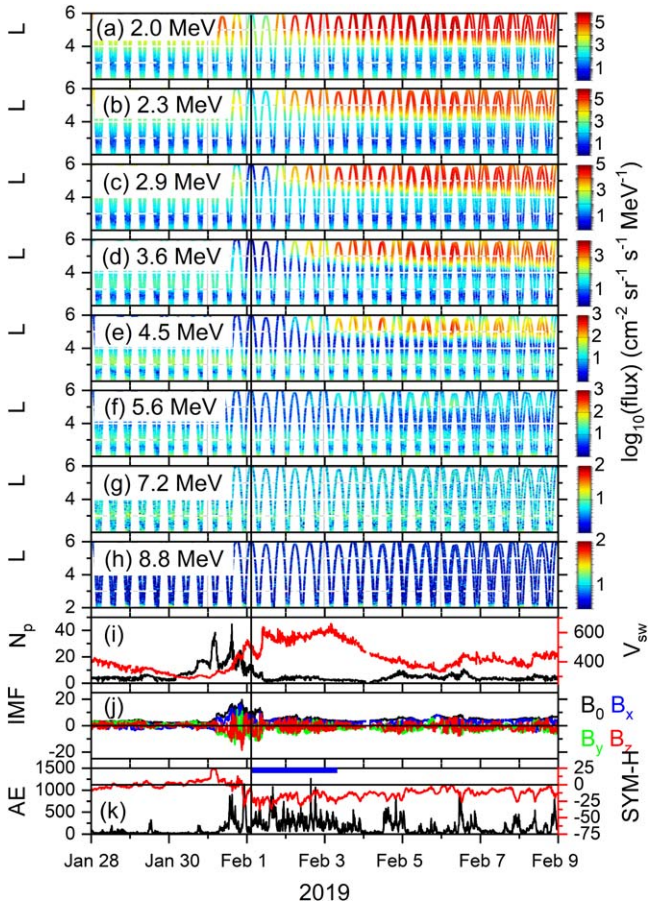

Figure 1. HILDCAA event and radiation belt electrons during 2019 January 28–February 8. (a)–(h) Fluxes of relativistic electrons with energies of ∼2.0–8.8 MeV, color-coded flux values are shown by color bars at the right; variations in (i) solar wind N_p (cm^{-3}, black, legend on the left) and V_{sw} (km s^{-1}, red, legend on the right); (j) IMF B_0, and B_x, B_y, and B_z (nT); (k) AE (nT, black, legend on the left) and SYM-H (nT, red, legend on the right) indices. The HILDCAA interval is indicated by a horizontal blue bar in the bottom panel during February 1–3. A vertical black line indicates the time of the onset of HILDCAA.

shadowing effect (West et al. 1972, 1981; Li et al. 1997; Kim et al. 2008; Ohtani et al. 2009; Hietala et al. 2014; Hudson et al. 2014); or (2) due to relativistic electron interaction with electromagnetic ion cyclotron (EMIC) waves (Thorne & Kennel 1971; Horne & Thorne 1998; Summers et al. 1998; Meredith et al. 2006; Tsurutani et al. 2016b; Hajra & Tsurutani 2018). Strong CIR ram pressure (not shown) compresses the dayside magnetospheric outer zone magnetic fields, making them blunter than a dipole configuration. Energetic electrons gradient drifting from the midnight to dawn sector will drift toward the magnetopause boundary and be lost to the magnetosheath. This is called magnetopause shadowing (West et al. 1972). This may lead to electron losses on open drift paths. Solar wind ram pressure enhancement can also excite EMIC waves in the dayside magnetosphere, and the cyclotron resonant interactions of the relativistic electrons with EMIC waves are shown to be a possible loss mechanism for these particles to the ionosphere (e.g., Remya et al. 2015; Tsurutani et al. 2016b).

About 1 day after the onset of HILDCAA, the ∼2.0 MeV electron fluxes start increasing at $L \geqslant 5.0$, followed by gradual flux increases at lower L shells, down to $L \sim 4.0$ (Figure 1(a)). Similar variations are noted for ∼2.3 to ∼4.5 MeV electrons

[9] https://rbspgway.jhuapl.edu/
[10] https://omniweb.gsfc.nasa.gov/

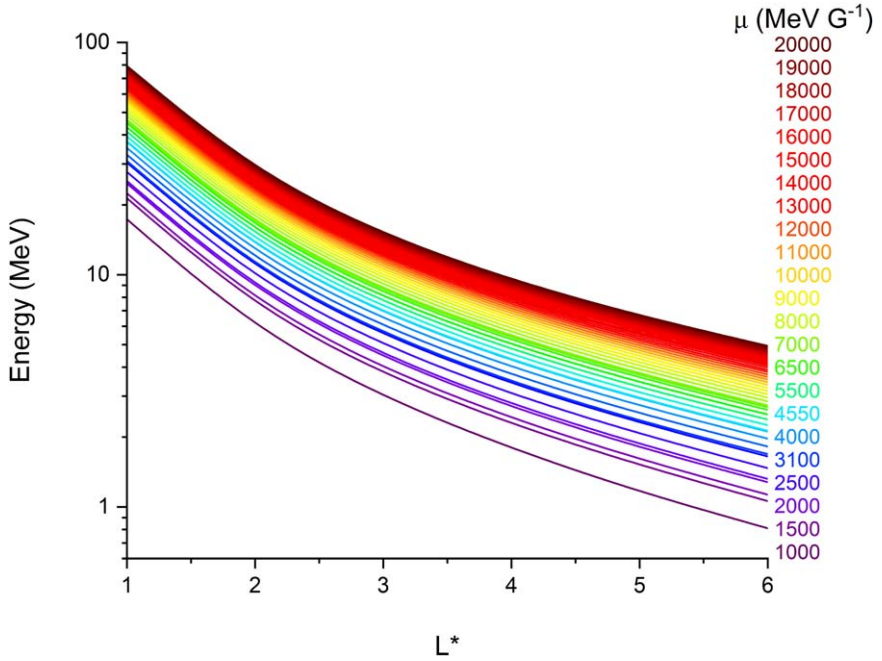

Figure 2. Variation in electron energy with L^* for various values of μ between 1000 and 20,000 MeV G^{-1} for $K = 0.11\ R_E\ G^{1/2}$ during 2019 January 28–February 8.

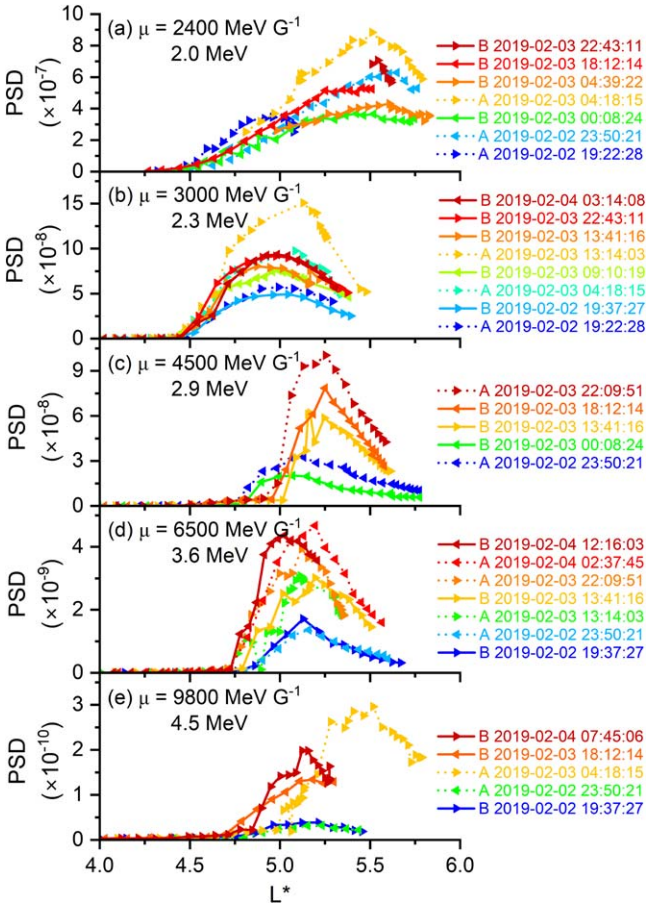

Figure 3. Superposed variations in PSD (c^3 cm^{-3} MeV^{-3}/PSDU) radial profiles measured by VAP A (dotted lines) and B (solid lines) for electrons with varying μ-values and $K = 0.11\ R_E\ G^{1/2}$ around the electron acceleration periods shown in Figure 1. Electron energies at $L^* = 4.5$–5.0 corresponding to the μ-values are mentioned in each panel. Inbound and outbound passes are marked by leftward and rightward triangles, respectively. Increasing dates and/or times are marked by colors from blue to red in each panel.

(Figures 1(b)–(e)). However, the ∼4.5 MeV fluxes increase only in a narrow region ($L \sim 5.0$–6.0), ∼2.5 days after the onset of HILDCAA (Figure 1(e)). It may be noted that we explored electrons of all energy levels (∼2–20 MeV) measured by VAPs. However, there are no significant flux enhancements for electrons with energy >4.5 MeV above their noise levels.

Figure 2 shows the L^*-shell variations in the electron energy for various μ-values between 1000 and 20,000 MeV G^{-1} for $K = 0.11\ R_E\ G^{1/2}$. The plot is based on data collected from 2019 January 28 to February 8. As clear from this figure, a specific μ corresponds to different energies at different L^* values. Thus, we explored a range of μ to study electron accelerations at different energies (Allison & Shprits 2020). For electron accelerations observed at $L^* \geqslant 4.5$–5.0 and shown in Figure 1, we considered the following μ-values (and corresponding electron energies): 2400 MeV G^{-1} (∼2.0 MeV), 3000 MeV G^{-1} (∼2.3 MeV), 4500 MeV G^{-1} (∼2.9 MeV), 6500 MeV G^{-1} (∼3.6 MeV), 9800 MeV G^{-1} (∼4.5 MeV), 14,600 MeV G^{-1} (∼5.6 MeV), and 23,300 MeV G^{-1} (∼7.2 MeV).

Figure 3 shows the electron PSDs (in PSD unit = c^3 cm^{-3} MeV^{-3}/PSDU, c is the speed of light) between $L^* = 4.0$ and 6.0 for constant μ- and K-values around the electron acceleration periods shown in Figure 1. Local peaks are prominent in all PSDs. More importantly, for a particular probe, the peak value is found to increase with time. For example, for $\mu = 3000$ MeV G^{-1}, which corresponds to 2.3 MeV electrons (Figure 3(b)), the outbound pass of VAP A at ∼19:22 UT on February 2, registered a peak PSD of $\sim 5.7 \times 10^{-8}$ PSDU at $L^* \sim 5.0$. At ∼04:18 UT on February 3, the outbound pass of VAP A registered a higher PSD peak of $\sim 9.7 \times 10^{-8}$ PSDU at $L^* \sim 5.1$. The peak is even higher, $\sim 15.1 \times 10^{-8}$ PSDU, located at $L^* \sim 5.1$, as noted by the outbound pass of VAP A at ∼13:14 UT on February 3. Considering VAP B, the PSD peak is found to increase systematically with time: $\sim 4.9 \times 10^{-8}$ PSDU ($L^* \sim 5.0$) at 19:37 UT on February 2, $\sim 7.4 \times 10^{-8}$ PSDU ($L^* \sim 5.0$) at

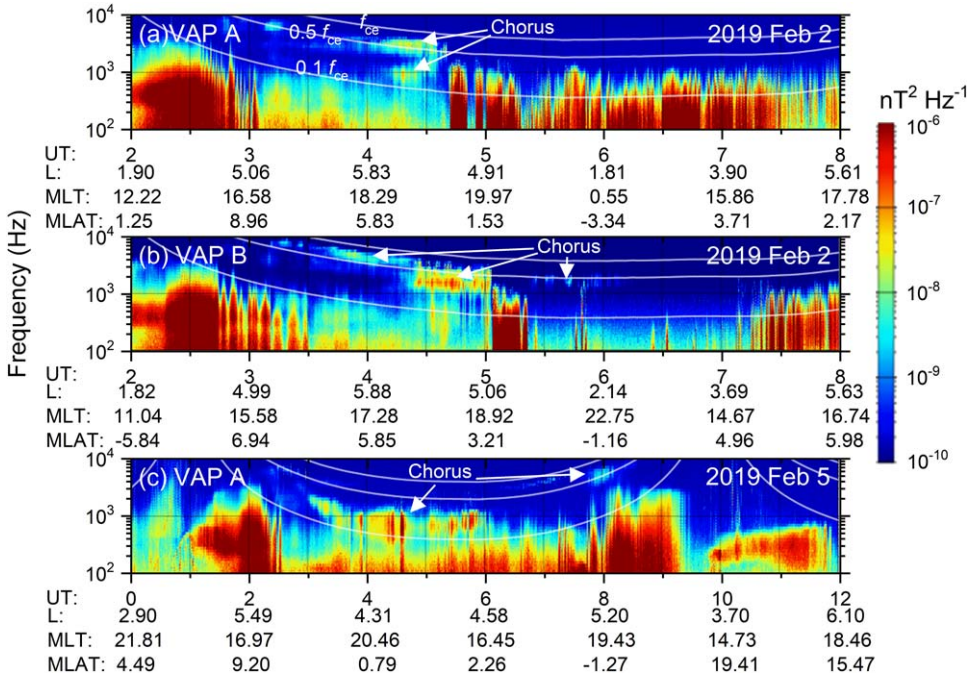

Figure 4. Magnetic spectral intensity (color scale on the right) of highly structured whistler-mode chorus waves as a function of frequency around the electron acceleration periods shown in Figure 1. Superimposed white lines demarcate the electron gyrofrequency f_{ce}, 0.5 f_{ce}, and 0.1 f_{ce} (from top to bottom, respectively).

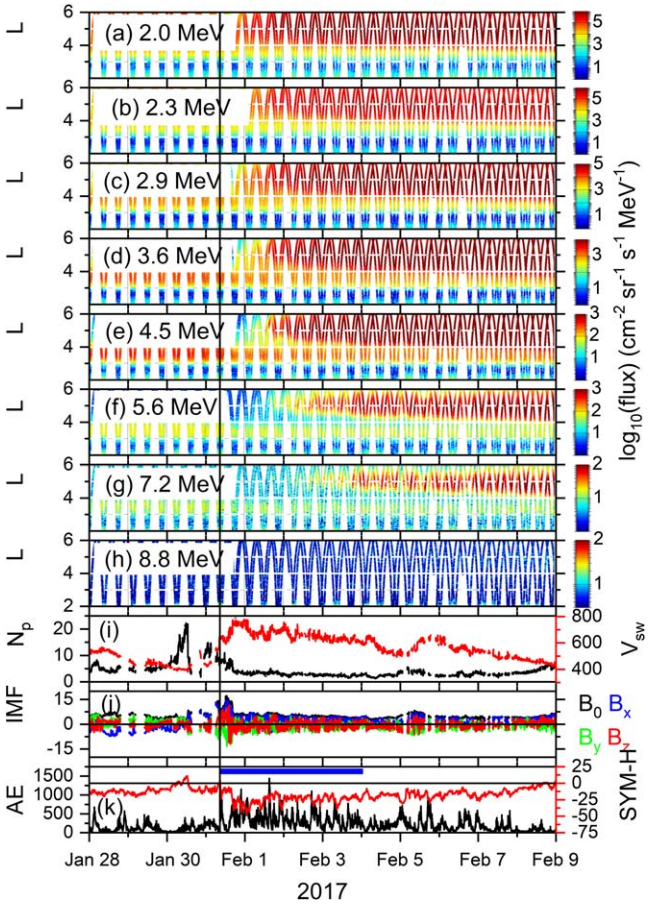

Figure 5. HILDCAA event and radiation belt electrons during 2017 January 28–February 8. The panels are in the same format as Figure 1.

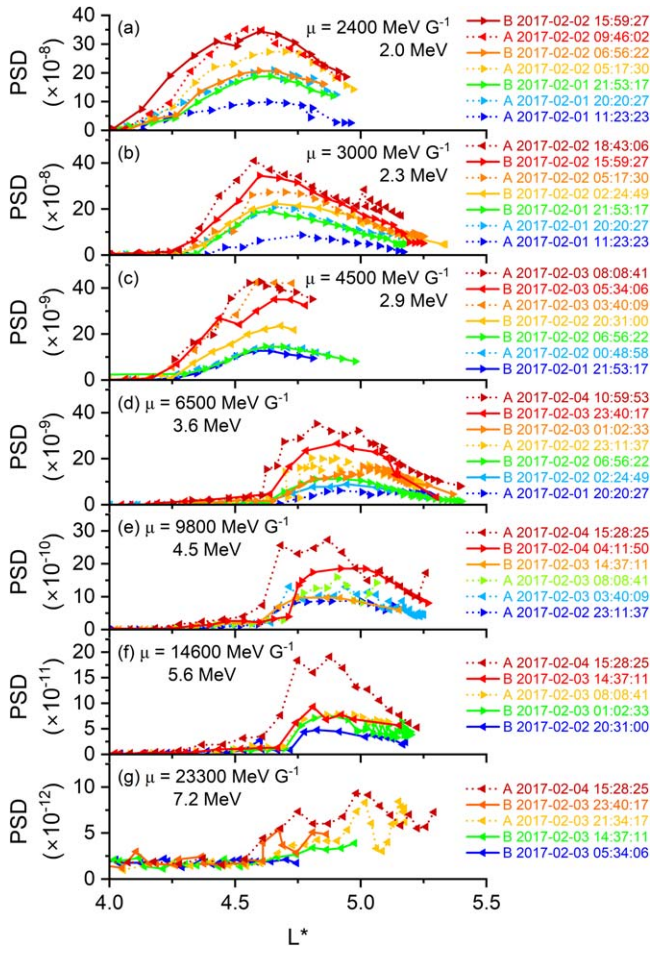

Figure 6. Superposed variations in PSD radial profiles for electron acceleration intervals shown in Figure 5. The panels are in the same format as Figure 3.

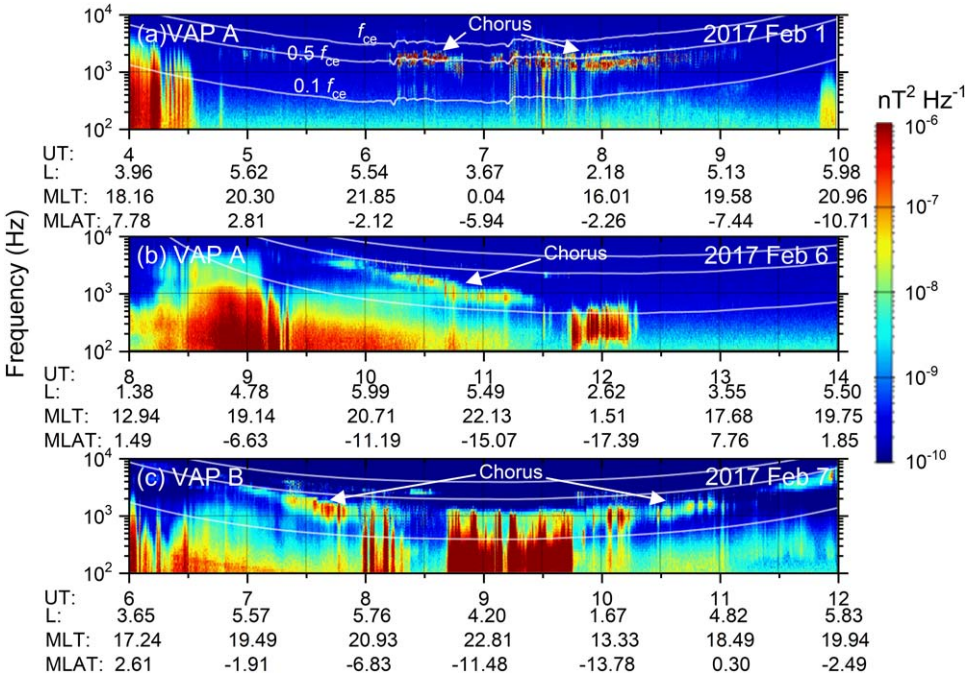

Figure 7. Magnetic spectral intensity of highly structured whistler-mode chorus waves as a function of frequency around the electron acceleration periods shown in Figure 5. The panels are in the same format as Figure 4.

09:10 UT on February 3, $\sim 8.0 \times 10^{-8}$ PSDU ($L^* \sim 4.9$) at 13:41 UT on February 3, $\sim 9.2 \times 10^{-8}$ PSDU ($L^* \sim 5.0$) at 22:43 UT on February 3, and $\sim 9.3 \times 10^{-8}$ PSDU ($L^* \sim 5.0$) at 03:14 UT on February 4. More or less similar, growing peak-PSD profiles (at $L^* \sim 4.5$–5.0) with negative gradients at higher L^*-values are observed for all μ-values, indicating a possible local acceleration of electrons at all energy levels.

Figure 4 shows the magnetic spectral intensity during the observed electron acceleration intervals (Figure 1). Strong magnetic spectral intensities indicate chorus waves excited over the frequency range (0.1–0.8) f_{ce} around the dusk sector at $L \sim$ 4.0–6.0. The presence of observed chorus waves is consistent with the electron acceleration to relativistic energies shown in Figure 1 (e.g., Horne et al. 2005, 2018).

Figure 5 shows another example of relativistic and ultra-relativistic electron accelerations associated with an HILDCAA event occurring during 2017 January 28–February 8. During this HILDCAA event, magnetospheric electrons are found to be accelerated up to a maximum energy of ~7.2 MeV (Figure 5(g)). The HILDCAA event is longer than the 2019 HILDCAA event shown in Figure 1. The electron flux enhancements are larger in magnitude and deeper in the magnetosphere (lower L-shells) compared to the 2019 case.

While the HILDCAA geomagnetic activity and associated solar/interplanetary variations during 2017 January 28–February 8 (the above Figure 5) are somewhat similar to the 2019 event (previous Figure 1), there are important differences that we wish to point out to the reader. The 2017 HILDCAA event (Figure 5) has a duration of ~3.69 days, an AE peak of ~1440 nT, and an integrated AE value of ~1285 nT day, respectively. These are significantly higher than the duration (~2.21 days), the AE peak (~1262 nT), and the integrated AE value (~658 nT day) of the 2019 HILDCAA event (Figure 1). The 2017 HSS (Figure 5) has a higher V_{sw} peak (~773 km s^{-1}), and a longer $V_{sw} > 500$ km s^{-1} duration (~4.60 days) compared to the 2019 HSS (Figure 1) peak V_{sw} (~661 km s^{-1}), and $V_{sw} > 500$ km s^{-1} duration (~2.54 days), respectively. These are consistent with ~7.2 MeV electron acceleration during the 2017 HILDCAA event compared to only ~4.5 MeV electron acceleration during the 2019 HILDCAA event assuming a bootstrap acceleration by chorus.

Figure 6 shows the electron PSDs around the electron acceleration intervals shown in Figure 5. The PSDs for all μ-values exhibit clear local peaks at $L^* \geqslant 4.5$–5.0, and the peak values increasing with time are indicative of a local acceleration of the electrons. Thus, the local acceleration of electrons seems to be a dominant process for the observed electron energization during the HILDCAA event (Figure 5).

Figure 7 shows examples of whistler-mode chorus waves during the observed electron acceleration (Figure 5). Chorus waves are observed between 0.1 and 0.8 f_{ce} at $L \sim$ 2.0–6.0 (Figure 7(a)), $L \sim$ 4.0–6.0 (Figure 7(b)), and $L \sim$ 5.0–6.0 (Figure 7(c)). Chorus are detected during local midnight and dusk sectors.

It can be noted that recent studies (e.g., Allison & Shprits 2020; Shprits et al. 2022) have reported the acceleration of electrons to ultra-relativistic energies, associated with strong geomagnetic storms. However, in the present work, we show ultra-relativistic electron acceleration during HILDCAA events, which are significantly different than strong geomagnetic storms. Strong storms are associated with long-duration, large-amplitude IMF B_s leading to intense inward convection and significant development of the ring current through magnetic reconnection (e.g., Gonzalez et al. 1994, 2007; Echer et al. 2008a, 2008b). On the other hand, HILDCAA is associated with the interplanetary Alfvén wave train (Tsurutani & Gonzalez 1987) characterized by a series of short-duration IMF B_s. During the magnetic reconnection associated with Alfvén wave B_s components, energetic particles are continuously injected into the large $L = 10$–4 region of the magnetosphere, and are lost without significant development of a ring current. However, the reconnection events excite strong

substorms in the auroral region, which comprise an HILDCAA event. Thus, the magnetosphere-ionosphere dynamics of the HILDCAA events are different from strong storms.

As mentioned in Section 2, we identified six suitable HILDCAA events to study during the entire VAP operation period. While two of the HILDCAA cases are discussed above, the parameters of the other cases are shown in detail in the Appendix. The main results obtained from detailed case studies of all the events are summarized in Table 1.

From Table 1 (based on Figures 1, 5, A1, A3, A5, and A7), ~3.4–4.1 days long HILDCAA events are found to be characterized by ~7.2 MeV electron acceleration in the $L \sim$ 4.0–6.0 region, ~2.9–3.4 days after the onset of HILDCAA. On the other hand, shorter (~2.2–2.5 days) HILDCAA events are associated with electron acceleration only up to ~4.5–5.6 MeV in the $L \sim$ 4.5–6.0 region, ~2.1–2.3 days after the onset of HILDCAA. In addition, the ~7.2 MeV electron acceleration is associated with longer-duration and faster HSSs compared to the cases with ~4.5–5.6 MeV electron acceleration. Thus, the duration of HILDCAA, and the duration and speed of HSSs seem to be important for ultra-relativistic electron acceleration. Longer-duration HSSs embedded with longer-duration Alfvén waves lead to continuous substorm and convection events or HILDCAA events that are longer duration. These can effectively and continuously generate chorus waves in the outer radiation belt, which in turn may lead to gradual local accelerations of the electrons. Growing local peaks at specific L^* values (and negative gradients at higher L^* values) observed in the radial PSD profiles of the electrons (Figures 3, 6, A2, A4, A6, and A8), and the magnetospheric chorus waves in the frequency range (0.1–0.8) f_{ce} observed during the HILDCAA events (Figures 4, and 7) are consistent with the local acceleration of the electrons.

4. Concluding Remarks

In this paper, we studied the variations in the Earth's outer radiation belt relativistic and ultra-relativistic electrons during HILDCAA events, which are associated with solar wind HSSs emanating from coronal holes. To summarize, the longer the duration of HILDCAA events, the higher the maximum energy of the relativistic electrons. For HILDCAA events of ~3.4–4.1 days, a maximum electron energy of ~7.2 MeV is found. This result indicates a clear relationship between the upper energy limit of magnetospheric relativistic electrons with the duration of an HILDCAA event. The present results are also consistent with the Hajra et al. (2015a) suggestion of a bootstrap acceleration mechanism, resulting in a longer delay for higher-energy electron acceleration from the onset of the HILDCAA event. In addition, our present findings indicate that local electron acceleration by chorus waves is the dominant acceleration mechanism during the HILDCAA events. For an interplanetary interval during 1973–1975 where two polar coronal holes (one in the north and one in the south; Tsurutani et al. 1995) existed causing continuous solar wind HSSs to impact the Earth's magnetosphere, one would certainly expect electron energies much higher than ~7.2 MeV. This could be a particular hazard for Earth-orbiting spacecraft.

Acknowledgments

The work of R.H. is funded by the "Hundred Talents Program" of the Chinese Academy of Sciences (CAS), and the Excellent Young Scientists Fund Program (Overseas) of the National Natural Science Foundation of China (NSFC). The work of Q.L. is supported by the NSFC grant No. 42230201. The VAP data are collected from the VAP Science Gateway.[11] The AE and SYM-H indices are obtained from the World Data Center for Geomagnetism, Kyoto, Japan.[12] The solar wind plasma and IMF data are collected from the OMNI web.[13] We would like to thank the reviewer for extremely valuable suggestions that substantially improved the manuscript.

Appendix
Additional Case Studies

Figures A1, A3, A5, and A7 show HILDCAA-related geomagnetic activity, causative solar wind and IMF variations, and associated outer radiation belt MeV electron variations. The results are summarized in Table 1. The electron PSD radial variations during the electron accelerations are shown in Figures A2, A4, A6, and A8.

The ~2.5 days long HILDCAA event during 2016 November 24–26, characterized by an AE peak of ~1837 nT was associated with an HSS with a peak V_{sw} of ~726 km s^{-1} (Figure A1). The event was characterized by a >2 orders of magnitude increase in the ~5.6 MeV fluxes, ~2.3 days after

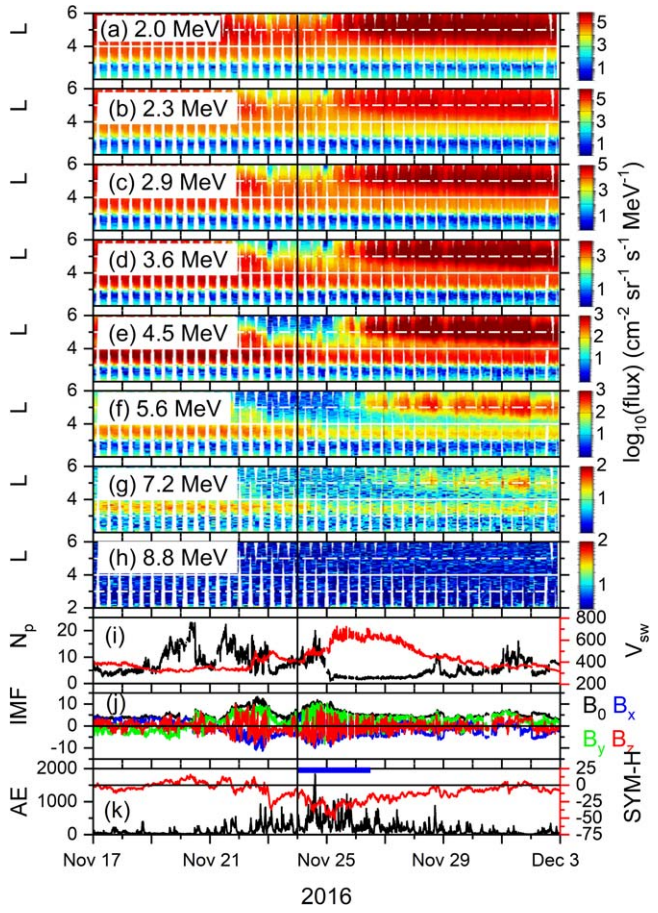

Figure A1. HILDCAA event and radiation belt electrons during 2016 November 17–December 2. (a)–(h) Fluxes of relativistic electrons with energies of ~2.0–8.8 MeV, color-coded flux values are shown by color bars at the right; variations in (i) solar wind N_p (cm^{-3}, black, legend on the left) and V_{sw} (km s^{-1}, red, legend on the right); (j) IMF B_0, and B_x, B_y, and B_z (nT); (k) AE (nT, black, legend on the left) and SYM-H (nT, red, legend on the right) indices. The HILDCAA interval is indicated by a horizontal blue bar in the bottom panel. A vertical black line indicates the onset time of HILDCAA.

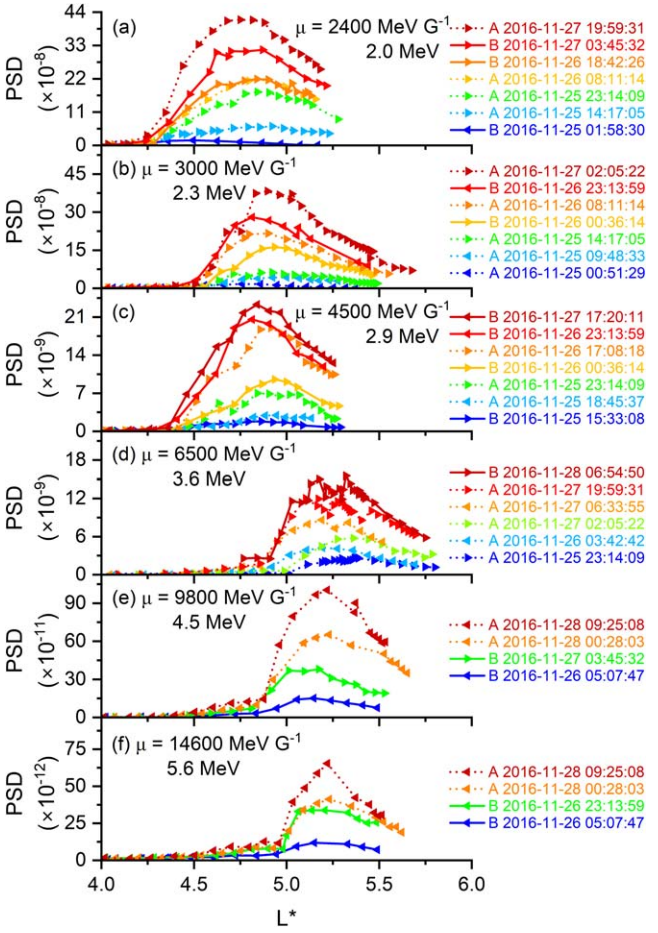

Figure A2. Superposed variations in PSD (c^3 cm^{-3} MeV^{-3}/PSDU) radial profiles measured by VAP A (dotted lines) and B (solid lines) for electrons with varying μ-values and $K = 0.11$ R_E $G^{1/2}$ around the electron acceleration periods shown in Figure A1. Electron energies at $L^* = 4.5$–5.0 corresponding to the μ-values are shown in each panel. Inbound and outbound passes are marked by leftward and rightward triangles, respectively. Increasing dates and/or times are marked by colors from blue to red in each panel.

the onset of HILDCAA. Analysis of the electron PSDs indicates local peaks, which are gradually increasing with time (Figure A2). The PSDs are indicative of local electron accelerations.

The ∼3.4 days long HILDCAA event during 2016 December 21–24 was characterized by an AE peak of ∼2231 nT, and occurred during an HSS with a peak V_{sw} of ∼775 km s^{-1} (Figure A3). The event was associated with a >2 orders of magnitude increase in the ∼7.2 MeV fluxes, ∼3.0 days after the onset of HILDCAA. The electron PSDs with growing local peaks (Figure A4) indicate local electron accelerations.

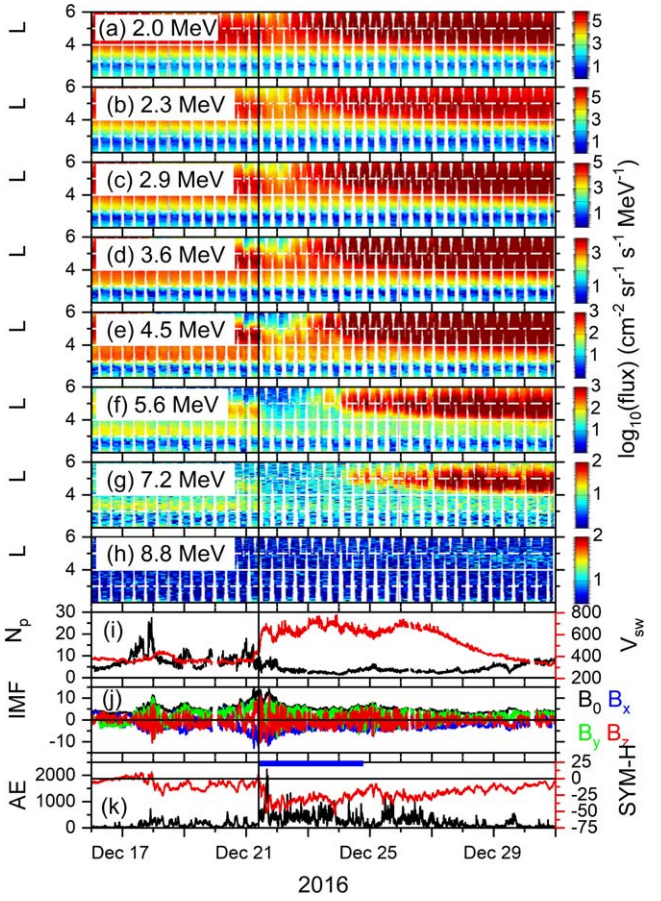

Figure A3. HILDCAA event and radiation belt electrons during 2016 December 16–30. The panels are in the same format as Figure A1.

The ∼4.1 days long HILDCAA event during 2017 August 17–21, characterized by an AE peak of ∼1847 nT occurred during an HSS with a peak V_{sw} of ∼769 km s^{-1} (Figure A5). The event was associated with a >2 orders of magnitude increase in the ∼7.2 MeV fluxes, ∼2.9 days after the onset of HILDCAA. Local electron accelerations are confirmed by growing local peaks in the electron PSD radial profiles (Figure A6).

The ∼2.6 days long HILDCAA event during 2019 February 28–March 2 was characterized by an AE peak of ∼1280 nT (Figure A7). It occurred during an HSS with a peak V_{sw} of ∼627 km s^{-1}. The event was associated with a >2 orders of magnitude increase in the ∼5.6 MeV fluxes, ∼2.1 days after the onset of HILDCAA. The electron PSD radial profiles are characterized by local peaks gradually increasing with time (Figure A8), indicative of local electron accelerations.

[11] https://rbspgway.jhuapl.edu/
[12] https://wdc.kugi.kyoto-u.ac.jp/
[13] https://omniweb.gsfc.nasa.gov/

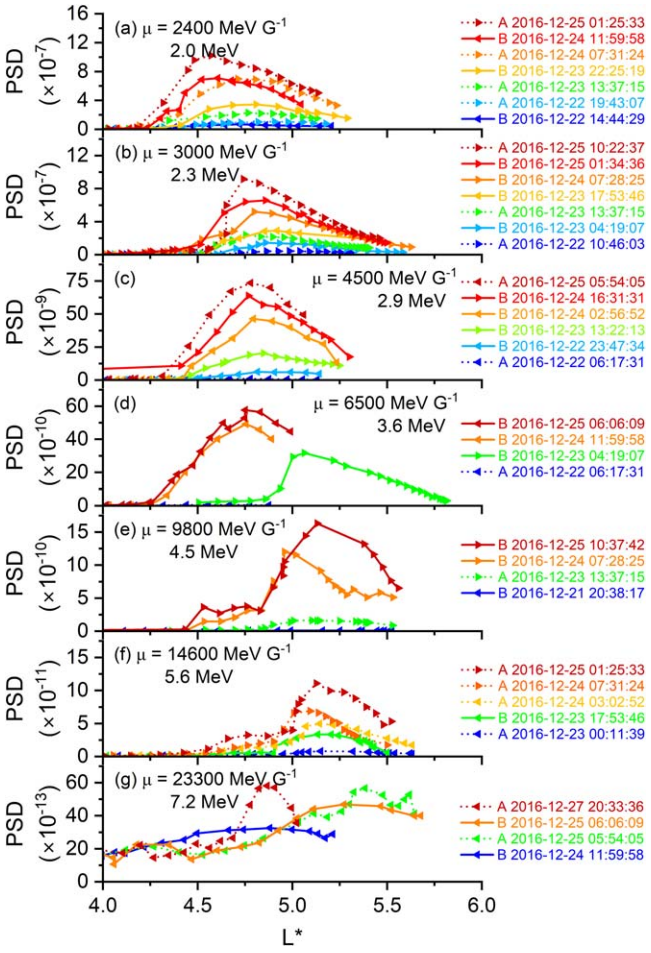

Figure A4. Superposed variations in PSD radial profiles for electron acceleration intervals shown in Figure A3. The panels are in the same format as Figure A2.

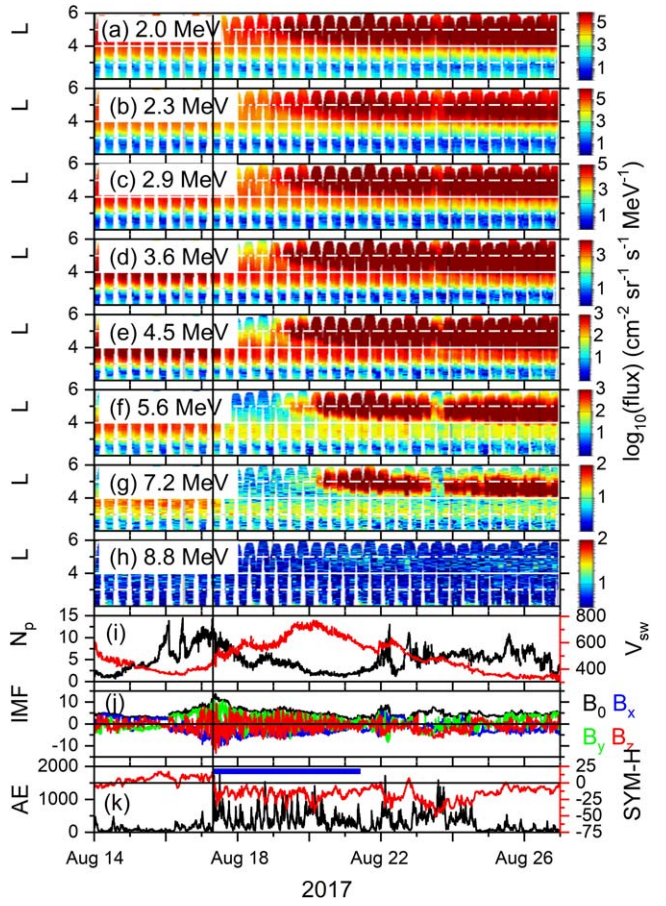

Figure A5. HILDCAA event and radiation belt electrons during 2017 August 14–26. The panels are in the same format as Figure A1.

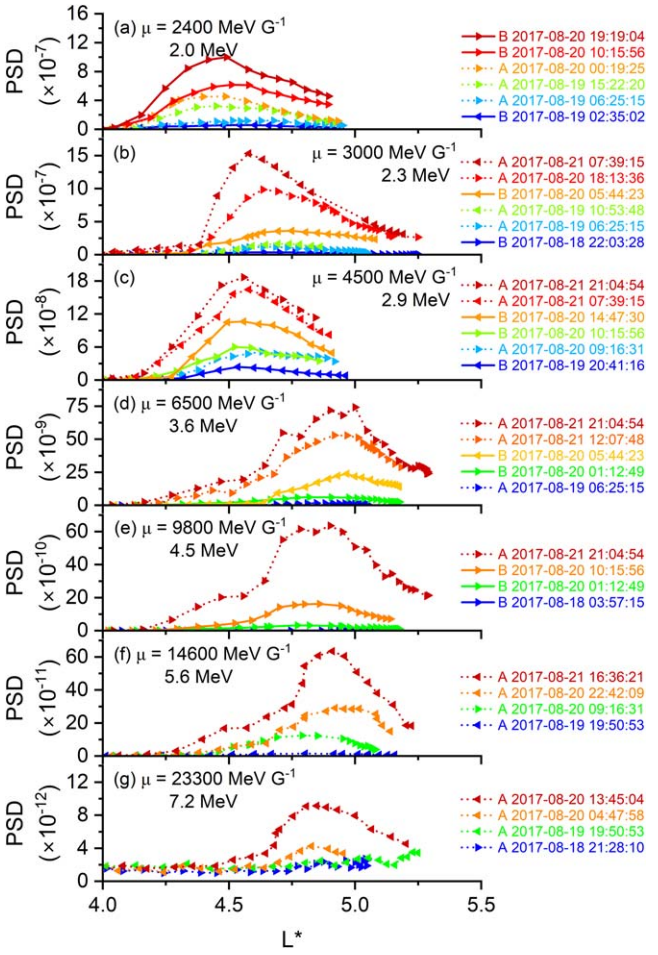

Figure A6. Superposed variations in PSD radial profiles for electron acceleration intervals shown in Figure A5. The panels are in the same format as Figure A2.

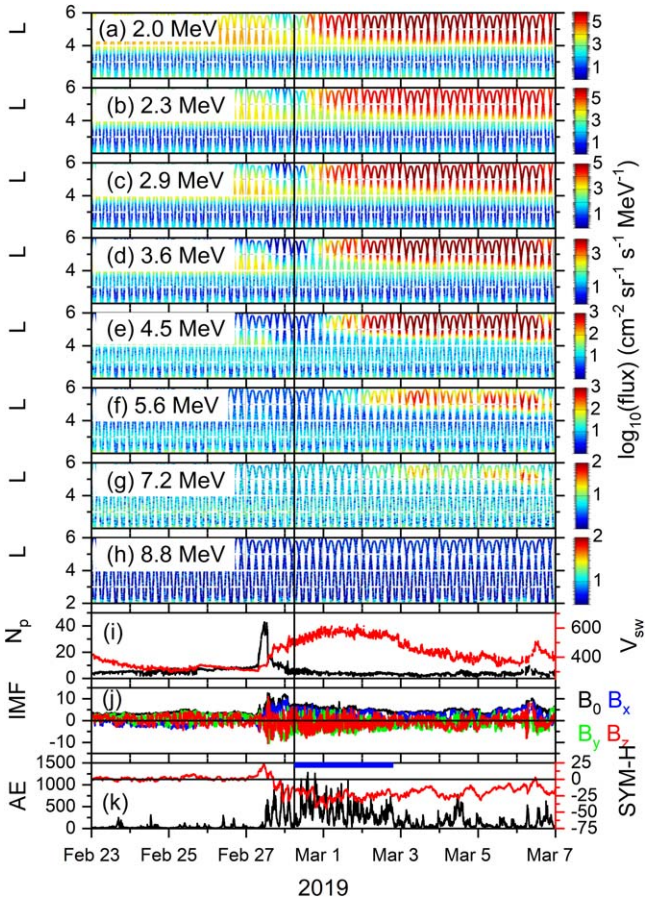

Figure A7. HILDCAA event and radiation belt electrons during 2019 February 23–March 6. The panels are in the same format as Figure A1.

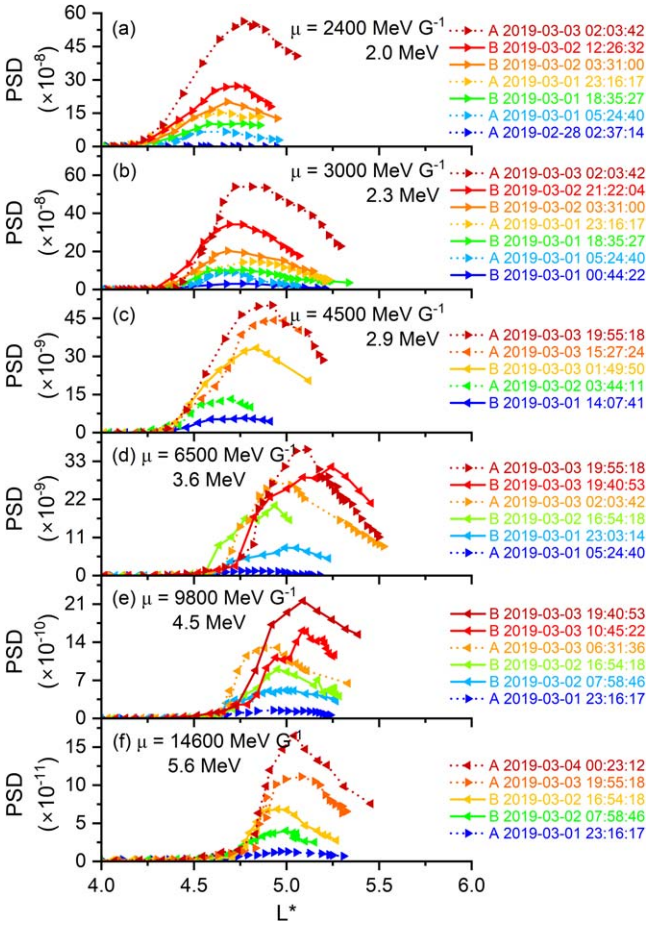

Figure A8. Superposed variations in PSD radial profiles for electron acceleration intervals shown in Figure A7. The panels are in the same format as Figure A2.

ORCID iDs

Rajkumar Hajra https://orcid.org/0000-0003-0447-1531
Bruce T. Tsurutani https://orcid.org/0000-0002-0094-7224
Quanming Lu https://orcid.org/0000-0003-3041-2682
Gurbax S. Lakhina https://orcid.org/0000-0002-8956-486X
Aimin Du https://orcid.org/0000-0002-0525-7898
Ezequiel Echer https://orcid.org/0000-0002-8351-6779
Adriane M. S. Franco https://orcid.org/0000-0003-0497-872X
Mauricio J. A. Bolzan https://orcid.org/0000-0002-4730-0102
Xinliang Gao https://orcid.org/0000-0003-0767-2267

References

Akasofu, S.-I. 1981, JGR, 86, 4820
Alfvén, H. 1950, Cosmical Electrodynamics (Oxford: Clarendon)
Ali, A. F., Malaspina, D. M., Elkington, S. R., et al. 2016, JGRA, 121, 9586
Allison, H. J., & Shprits, Y. Y. 2020, NatCo, 11, 4533
Baker, D. N., Jaynes, A. N., Li, X., et al. 2014, GeoRL, 41, 1351
Baker, D. N., Kanekal, S. G., Hoxie, V. C., et al. 2013, SSRv, 179, 337
Belcher, J. W., & Davis, L. 1971, JGR, 76, 3534
Bellan, P. M. 2013, PhPl, 20, 042117
Boyd, A. J., Spence, H. E., Claudepierre, S. G., et al. 2014, GeoRL, 41, 2275
Boyd, A. J., Turner, D. L., Reeves, G. D., et al. 2018, GeoRL, 45, 5253
DeForest, S. E., & McIlwain, C. E. 1971, JGR, 76, 3587
Dungey, J. W. 1961, PhRvL, 6, 47
Echer, E., Gonzalez, W. D., & Tsurutani, B. T. 2008a, GeoRL, 35, L06S03
Echer, E., Gonzalez, W. D., Tsurutani, B. T., & Gonzalez, A. L. C. 2008b, JGRA, 113, A05221
Elkington, S. R., Hudson, M. K., & Chan, A. A. 1999, GeoRL, 26, 3273
Fälthammar, C. G. 1965, JGR, 70, 2503
Foster, J. C., Erickson, P. J., Baker, D. N., et al. 2014, GeoRL, 41, 20
Gonzalez, W. D., Echer, E., Clua-Gonzalez, A. L., & Tsurutani, B. T. 2007, GeoRL, 34, L06101
Gonzalez, W. D., Joselyn, J. A., Kamide, Y., et al. 1994, JGR, 99, 5771
Green, J. C., & Kivelson, M. G. 2004, JGR, 109, A03213
Guarnieri, F. L. 2006, in Recurrent Magnetic Storms: Corotating Solar Wind Streams, ed. B. T. Tsurutani et al. (Washington, DC: American Geophysical Union), 235
Guarnieri, F. L., Tsurutani, B. T., Vieira, L. E. A., et al. 2018, NPGeo, 25, 67
Guo, D., Xiang, Z., Ni, B., et al. 2021, GeoRL, 48, e2021GL095714
Guo, D., Xiang, Z., Ni, B., et al. 2023, JGRA, 128, e2023JA031407
Hajra, R. 2021a, SoPh, 296, 50
Hajra, R. 2021b, AnGeo, 39, 181
Hajra, R., Echer, E., Tsurutani, B. T., & Gonzalez, W. D. 2013, JGRA, 118, 5626
Hajra, R., Echer, E., Tsurutani, B. T., & Gonzalez, W. D. 2014a, JASTP, 121, 24
Hajra, R., Tsurutani, B. T., Echer, E., & Gonzalez, W. D. 2014b, GeoRL, 41, 1876
Hajra, R., & Sunny, J. V. 2022, SoPh, 297, 30
Hajra, R., Sunny, J. V., Babu, M., & Nair, A. G. 2022, SoPh, 297, 97
Hajra, R., & Tsurutani, B. T. 2018, in Extreme Events in Geospace, ed. N. Geospace (Amsterdam: Elsevier), 373
Hajra, R., Tsurutani, B. T., Echer, E., Gonzalez, W. D., & Santolik, O. 2015a, ApJ, 799, 39
Hajra, R., Tsurutani, B. T., Echer, E., et al. 2015b, EP&S, 67, 109
Hajra, R., Tsurutani, B. T., & Lakhina, G. S. 2020, ApJ, 899, 3
Hietala, H., Kilpua, E. K. J., Turner, D. L., & Angelopoulos, V. 2014, GeoRL, 41, 2258
Horne, R. B., Glauert, S. A., & Thorne, R. M. 2003, GeoRL, 30, 1493
Horne, R. B., Phillips, M. W., Glauert, S. A., et al. 2018, SpWea, 16, 1202
Horne, R. B., & Thorne, R. M. 1998, GeoRL, 25, 3011
Horne, R. B., Thorne, R. M., Glauert, S. A., et al. 2005, JGR, 110, A03225
Hua, M., Bortnik, J., Chu, X., Aryan, H., & Ma, Q. 2022a, GeoRL, 49, e2022GL101096
Hua, M., Bortnik, J., & Ma, Q. 2022b, GeoRL, 49, e2022GL099618
Hudson, M. K., Baker, D. N., Goldstein, J., et al. 2014, GeoRL, 41, 1113
Hudson, M. K., Elkington, S. R., Lyon, J. G., Goodrich, C. C., & Rosenberg, T. J. 1999, in Sun-Earth Plasma Connections, ed. J. L. Burch, R. L. Carovillano, & S. K. Antiochos (Washington, DC: American Geophysical Union)
Inan, U. S., Bell, T. F., & Helliwell, R. A. 1978, JGR, 83, 3235
Jaynes, A. N., Ali, A. F., Elkington, S. R., et al. 2018, GeoRL, 45, 10874
Kanekal, S. G., Baker, D. N., Henderson, M. G., et al. 2015, JGRA, 120, 7629
Kennel, C. F., & Petschek, H. E. 1966, JGR, 71, 1
Kim, K. C., Lee, D. Y., Kim, H. J., et al. 2008, JGRA, 113, A09212
Kletzing, C. A., Kurth, W. S., Acuna, M., et al. 2013, SSRv, 179, 127
Lakhina, G. S., Tsurutani, B. T., Verkhoglyadova, O. P., & Pickett, J. S. 2010, JGRA, 115, A00F15
Li, W., Ma, Q., Thorne, R. M., et al. 2016, JGRA, 121, 5520
Li, W., Thorne, R. M., Ma, Q., et al. 2014, JGRA, 119, 4681
Li, X., Baker, D. N., Temerin, M., et al. 1997, JGR, 102, 14123
Li, X., & Temerin, M. A. 2001, SSRv, 95, 569
Lu, Q., Ke, Y., Wang, X., et al. 2019, JGRA, 124, 4157
Mann, I. R., O'Brien, T. P., & Milling, D. K. 2004, JASTP, 66, 187
Mauk, B. H., Fox, N. J., Kanekal, S. G., et al. 2013, SSRv, 179, 3
McIlwain, C. E. 1961, JGR, 66, 3681
Mendes, O., Domingues, M. O., Echer, E., Hajra, R., & Menconi, V. E. 2017, NPGeo, 24, 407
Meredith, N. P., Horne, R. B., & Anderson, R. R. 2001, JGR, 106, 13165
Meredith, N. P., Horne, R. B., Glauert, S. A., et al. 2006, JGRA, 111, A05212
Miyoshi, Y., Jordanova, V. K., Morioka, A., & Evans, D. S. 2004, SpWea, 2, S10S02
Morley, S. K., Henderson, M. G., Reeves, G. D., Friedel, R. H. W., & Baker, D. N. 2013, GeoRL, 40, 4798
Mourenas, D., Agapitov, O. V., Artemyev, A. V., & Zhang, X.-J. 2022, JGRA, 127, e2022JA030661
Mourenas, D., Artemyev, A. V., & Zhang, X.-J. 2019, JGRA, 124, 4445
Mourenas, D., Zhang, X. J., Artemyev, A. V., et al. 2018, JGRA, 123, 4979
Nishida, A. 1968, JGR, 73, 5549
Ohtani, S., Miyoshi, Y., Singer, H. J., & Weygand, J. M. 2009, JGRA, 114, A01202

Olifer, L., Mann, I. R., Ozeke, L. G., Morley, S. K., & Louis, H. L. 2021, GeoRL, 48, e2020GL092351
Ozeke, L. G., Mann, I. R., Olifer, L., et al. 2020, JGRA, 125, e2019JA027179
Reeves, G. D., Spence, H. E., Henderson, M. G., et al. 2013, Sci, 341, 991
Remya, B., Tsurutani, B. T., Reddy, R. V., Lakhina, G. S., & Hajra, R. 2015, JGRA, 120, 7536
Roederer, J. G. 1970, Dynamics of Geomagnetically Trapped Radiation (Berlin: Springer)
Schiller, Q., Tu, W., Ali, A. F., et al. 2017, JGRA, 122, 3354
Schulz, M., & Lanzerotti, L. 1974, Particle Diffusion in the Radiation Belts (Berlin: Springer)
Shprits, Y. Y., Allison, H. J., Wang, D., et al. 2022, JGRA, 127, e2021JA030214
Smith, E. J., & Wolfe, J. H. 1976, GeoRL, 3, 137
Souza, A. M., Echer, E., Bolzan, M. J. A., & Hajra, R. 2016, JASTP, 149, 81
Souza, A. M., Echer, E., Bolzan, M. J. A., & Hajra, R. 2018, AnGeo, 36, 205
Summers, D., Ni, B., & Meredith, N. P. 2007, JGRA, 112, A04207
Summers, D., Thorne, R. M., & Xiao, F. 1998, JGRA, 103, 20487
Sunny, J. V., Nair, A. G., Babu, M., & Hajra, R. 2023, AdSpR, 71, 268
Thorne, R. M. 2010, GeoRL, 37, L22107
Thorne, R. M., & Kennel, C. F. 1971, JGR, 76, 4446
Thorne, R. M., Li, W., Ni, B., et al. 2013, Natur, 504, 411
Thorne, R. M., O'Brien, T. P., Shprits, Y. Y., Summers, D., & Horne, R. B. 2005, JGRA, 110, A09202
Tsurutani, B. T., & Gonzalez, W. D. 1987, P&SS, 35, 405
Tsurutani, B. T., Gonzalez, W. D., Gonzalez, A. L. C., et al. 1995, JGR, 100, 21717
Tsurutani, B. T., Gonzalez, W. D., Gonzalez, A. L. C., et al. 2006a, JGRA, 111, A07S01
Tsurutani, B. T., McPherron, R. L., Gonzalez, W. D., et al. 2006b, in Recurrent Magnetic Storms: Corotating Solar Wind Streams, ed. B. T. Tsurutani et al. (Washington, DC: American Geophysical Union), 1
Tsurutani, B. T., Gould, T., Goldstein, B. E., Gonzalez, W. D., & Sugiura, M. 1990, JGR, 95, 2241
Tsurutani, B. T., Hajra, R., Echer, E., Gonzalez, W. D., & Santolik, O. 2016a, NASA Tech Briefs, 40, 20, https://www.techbriefs.com/component/content/article/24815-npo-49852
Tsurutani, B. T., Hajra, R., Tanimori, T., et al. 2016b, JGRA, 121, 10130
Tsurutani, B. T., Horne, R. B., Pickett, J. S., et al. 2010, JGRA, 115, A00F01
Tsurutani, B. T., & Lakhina, G. S. 1997, RvGeo, 35, 491
Tsurutani, B. T., Lakhina, G. S., Pickett, J. S., et al. 2005, NPGeo, 12, 321
Tsurutani, B. T., Lakhina, G. S., & Verkhoglyadova, O. P. 2013, JGRA, 118, 2296
Tsurutani, B. T., & Meng, C.-I. 1972, JGR, 77, 2964
Tsurutani, B. T., & Smith, E. J. 1977, JGR, 82, 5112
Tsurutani, B. T., Smith, E. J., West, H. I., & Buck, R. M. 1979, in Waves Instabilities in Space Plasmas, ed. P. J. Palmadesso & K. Papadopoulos (Dordrecht: Springer), 55
Tsurutani, B. T., Verkhoglyadova, O. P., Lakhina, G. S., & Yagitani, S. 2009, JGR, 114, A03207
Tsyganenko, N. A., & Sitnov, M. I. 2005, JGRA, 110, A03208
West, H., Buck, R., & Walton, J. 1972, NPhS, 240, 6
West, H. I., Buck, R. M., & Davidson, G. T. 1981, JGR, 86, 2111
Xiao, F., Yang, C., He, Z., et al. 2014, JGRA, 119, 3325
Yoon, D. Y., & Bellan, P. M. 2020, JGRA, 125, e2020JA027796
Zhao, H., Baker, D. N., Li, X., Jaynes, A. N., & Kanekal, S. G. 2018, GeoRL, 45, 5818
Zhao, H., Baker, D. N., Li, X., et al. 2019, JGRA, 124, 8590
Zong, Q. G., Zhou, X. Z., Wang, Y. F., et al. 2009, JGR, 114, A10204